



Investigation of a four-bladed propeller inflow at yaw

Ross J. Higgins, Angel Zarev, Richard B. Green, George N. Barakos*

University of Glasgow, Glasgow, Scotland, G12 8QQ, United Kingdom

ARTICLE INFO

Article history:

Received 5 January 2022
 Received in revised form 30 March 2022
 Accepted 30 March 2022
 Available online 1 April 2022
 Communicated by Grigorios Dimitriadis

Keywords:

CFD
 Propeller
 Inflow
 LDA

ABSTRACT

An investigation has been conducted which looks to understand the effect of yaw on the inflow of a 4-bladed propeller. Both experimental and numerical work has been conducted, with the test data used to validate and compare against the numerical methods. The numerical methods involve fully resolved CFD and the low-order Crigler method. Comparing at a yaw angle of 15°, good agreement is found between the numerical and experimental results with adjustments made to account for discrepancies between the setups. More work is still required in the experimental and numerical branches to improve the extraction of data with minimal losses and improve the fidelity of simpler methods without a great expansion of computer cost.

© 2022 The Author(s). Published by Elsevier Masson SAS. This is an open access article under the CC BY license (<http://creativecommons.org/licenses/by/4.0/>).

1. Introduction

With the rise of electric propulsion and experimental aircraft, propellers are more frequently pushed towards operating regimes outside traditional configurations with the mainly axial flow, and into regimes where the inflow can no longer be assumed as perpendicular to the propeller disk. Examples range in duration and extent from aeroplane climb and descent manoeuvres, through cross-wind operations, cross-rotor flow interactions, tilt-rotor conversion flights and regular flights for multi-rotor drone propeller configurations. These are furthermore regimes that can be simulated by aircraft-aircraft interaction, flow velocity gradients such as those between fuselage, nacelle or wings with the propeller inflow.

While experimental literature on this topic is scarce, past works in the field can be divided into two main groups, with the first conducted pre-World War 2 [1–6]. The main focus of these studies was the measurement of averaged forces and moments to determine aircraft stability and performance.

Correspondingly, the notable findings of these works include the behaviour of propeller efficiency coefficients, the correlations between thrust and advance ratio at yaw, and most notably, the finding of additional forces and moments that arise in association with the inclination of the thrust axis to the airflow.

The second set of publications appeared between the 1940s and the 1960s, [7–12] considering more in-depth/detailed aspects of non-axial flight, such as structural effects and wake aerodynamics.

The initial works of Pendley [8] and Russell [10,11] found discrepancies between analytical and experimental loads. Conclusions drawn from these studies found an azimuthal shift in the propeller wake potentially impacting the derived loads. The later studies by Gray [7], McLemore [9] and Yaggi [12] found oscillating airloads to have a significant impact when the propeller is at yaw.

Due to the technology of their time, those studies were constrained by several factors. These include, but are not limited to, restricted temporal and geometric data resolution, lack of a well-populated experimental envelope in some cases, and limited data accuracy. With the development of non-interfering techniques, such as LDA, an opportunity for a better understanding of propellers at yaw is available.

To further develop the understanding of propellers at yaw, an experimental [13] and numerical [14] campaign has been conducted at the University of Glasgow. The initial experimental investigation involved the extraction of Laser Doppler Anemometry (LDA) data at the inflow of a two-bladed propeller. Subsequently, this study was able to provide validation data for the numerical investigation where additional findings such as skin friction and induced angle of attack effects of yaw were obtained.

Owing to the growth of computational capabilities in the last decades, and their comparative lower cost to experiments, a significant increase in the utilisation of Computational Fluid Dynamics (CFD) has been observed. This is true across all aerospace applications like propellers [15], helicopter rotors [16], wind turbines [17], aero-engines [18] and more. This, subsequently, led to the numerical investigation of the two-bladed propeller at yaw [14].

In terms of non-CFD models, it is found that many of the widely available low order solvers still work under the assumption of uniform induced flow across the propeller disc, set out by de Young

* Corresponding author.

E-mail address: george.barakos@glasgow.ac.uk (G.N. Barakos).

Nomenclature

$a_{[a,r,\omega]}$	Induction factors [axial, radial and tangential].....	–
D	Propeller diameter.....	m
J	Advance ratio, $J = V_\infty/nD$	–
n, ω	Propeller rotational speed.....	revolutions/s, radians/s
R, r	Propeller radius, propeller radial position.....	m, –
$Re_{0.7}$	Reynolds number (based on advancing blade 0.7R position and chord).....	–
$V_{[\infty,R]}$	Velocity [freestream, resultant].....	m/s
$V_{axial(LDA)}$	LDA measured velocity perpendicular to the propeller plane.....	m/s
$V_{[n,p]}$	Freestream velocity components w.r.t. the propeller disc [normal, perpendicular].....	m/s

α_R	Blade component resultant angle of attack.....	°
$\beta_{0.7}$	Pitch angle at 0.7R.....	°
γ	Yaw angle.....	°
φ	Blade component advance angle.....	°
ψ	Blade azimuthal position.....	°

Acronyms

CFD	Computational Fluid Dynamics
LDA	Laser Doppler Anemometry
WT	Wind Tunnel

in 1965 [19], or the steady-state assumption defined by Crigler in 1952 [20]. An improvement on these models was derived in 1980 by Pitts and Peters [21,22], where the induced velocity at the propeller plane is calculated based upon a truncated Fourier series and works under the assumption of the superposition of pressure. Studies have been conducted in recent times [23] with consistent results of forces and moments found in axial and yawed test conditions whilst using the Pitts and Peters model. The Pitts and Peters is a dynamic inflow model and it requires additional coupling to a blade element like model to obtain propeller blade loads. Such a model can provide an accurate solution at a low cost, however, it is reliant upon an accurate initial flow solution.

The focus of the current paper is to extend the findings found from the previous experimental and numerical campaigns [13,14] to understand the change in aerodynamic profile through the propeller disc. For this, a four-bladed experimental study was conducted to ensure uniformity of the loads and was used as a validation test case for the CFD. Following this validation, a range of additional profiles upstream and downstream of the propeller blade are extracted from the CFD with the trends examined at yaw. At the same time, existing engineering approaches are compared with both CFD and test data.

2. Methodology

2.1. Experiment

A thorough description of the experimental methodology can be found [13], with the key elements summarised here. The experimental data for the study was acquired in the University of Glasgow De Havilland wind tunnel facility. The measurements were conducted using a Dantec Dynamics three-component Laser Doppler Anemometry (LDA) system, focusing 3 cm upstream of the hub and propeller centre. The experimental plane consisted of a coordinate grid of 360 points, each containing 36 azimuthal and 10 radial positions, with a measurement time of 3 s. In terms of the experimental blade setup, the reference pitch at 70%R was measured via an inclinometer with a tolerance of $\pm 0.1^\circ$. Presented in Fig. 1 is the experimental setup in the De Havilland wind tunnel.

The propeller hub was rigid and non-articulated, with a total diameter including the propellers of 0.499 m. The motor powering the main rig was a Lenze MCS09L41 1.9 KW synchronous servo motor paired with a programmable driver. The rated maximum continuous operation frequency was 4050 revolutions per minute, with a rated and peak torque of 7.5 and 32 Nm, respectively.

In addition to the inflow LDA data, force acquisition was performed using an AMTI MC5-1250 load cell. The resonance frequency was confirmed to be significantly above the experimental spectrum via vibrometer testing. Tare correction was automatically applied by the measuring system and the load cell software.

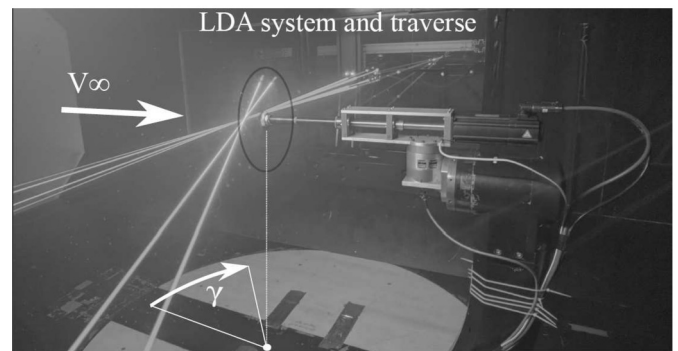


Fig. 1. Experimental setup for the extraction of LDA inflow and load data for the propeller at yaw.

Table 1

Summary of selected experimental set test conditions.

Test Case	$V_\infty = 30$ m/s, $\gamma = 15^\circ$
Blade Count	4
Freestream Reynolds Number (-)	0.034×10^6
Tip Velocity (m/s)	61.21
Propeller Rotational Velocity (rpm)	2385
Inflow Velocity (m/s)	30.0
Inflow Yaw Angle (°)	15.0
Ambient Temperature (°C)	27.4
Speed of Sound (m/s)	347.51
Reduced Frequency (-)	0.0883
Blade Pitch Angle (°) _{0.70R}	49
Reference Chord Length (mm)	21.19
Blade Radius (m)	0.245
Time-step (°/step)	1.0

A range of conditions were investigated including yaw angles 0° to 20° . For this investigation, the focus is on the case of $V_\infty = 30$ m/s, $\gamma = 15^\circ$. This was selected based upon the cleanliness of the data extraction with reflections being more of an issue of the 4-bladed propeller compared to the 2-bladed. The test conditions are summarised in Table 1.

2.2. CFD

For the numerical investigation of propeller flows at yaw, the in-house CFD solver Helicopter-Multi-Block-3 (HMB3) is used. The core functionality of HMB3 is CFD, however, its use has been extended in recent years to incorporate different simulation tools. These include helicopter rotor aeroelasticity [24], propeller aero-

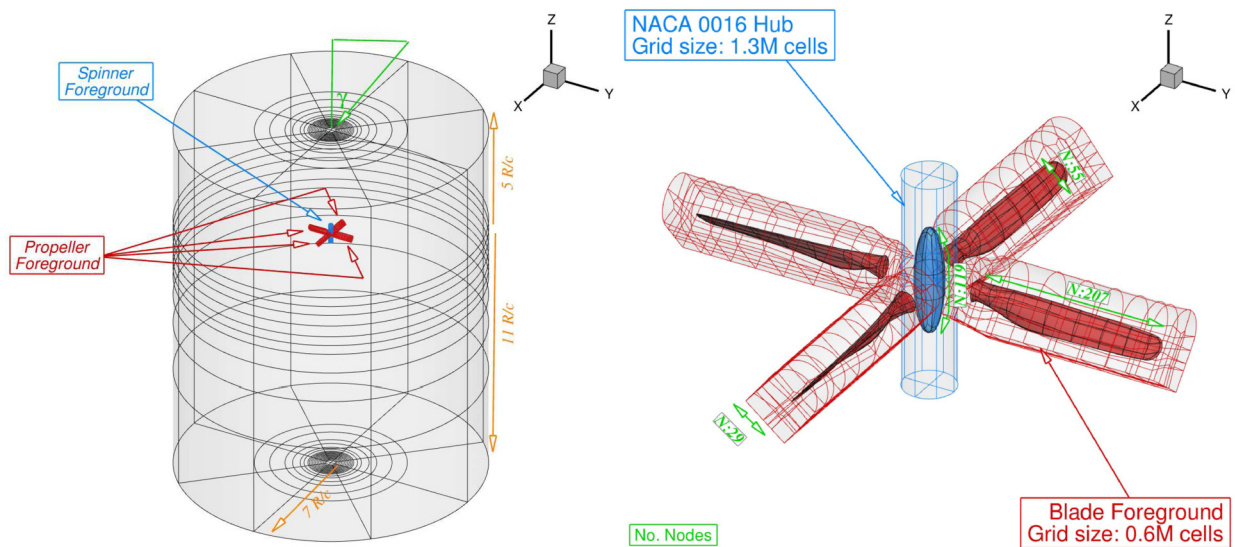


Fig. 2. Full computational grid including the blade and hub foreground components and cylindrical background. (For interpretation of the colours in the figure(s), the reader is referred to the web version of this article.)

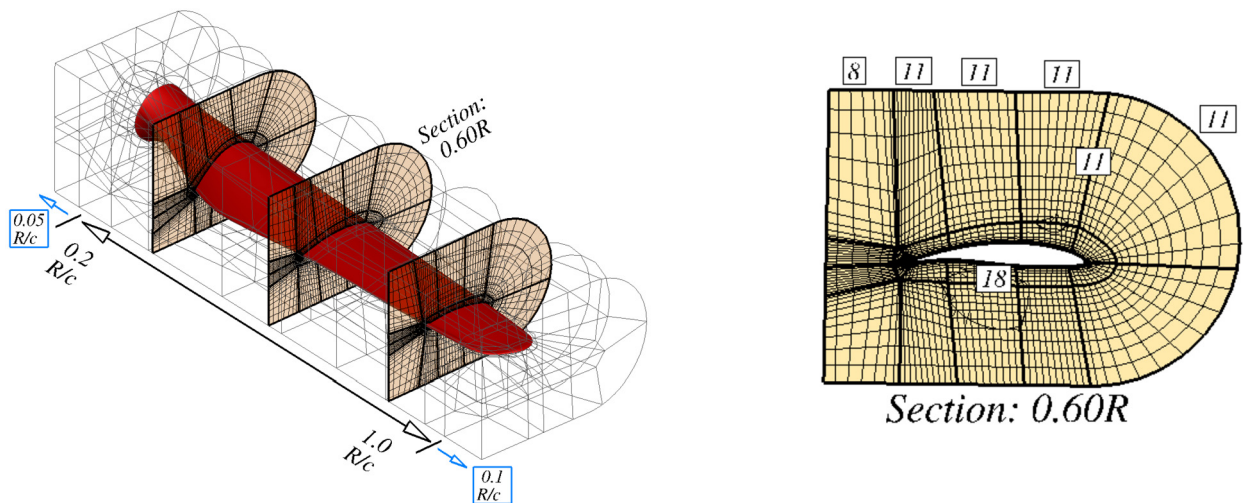


Fig. 3. Blade foreground grid with a sectional slice detailing the cell distribution data.

coustics [15], flight mechanics [25] and missile trajectory prediction [26]. Previous investigations using HMB3 have provided propeller flow validation in both installed and isolated conditions, by comparison with the experimental results of the Joint Open Rotor Propeller (JORP) blade [27] and the Improving the Propulsion Aerodynamic and aCoustics of Turboprop Aircraft (IMPACTA) wind tunnel tests [28,29]. These results were compared in 2016 [30] and 2018 [15], respectively, with good agreement found in terms of aerodynamics and acoustics.

As per the experimental setup, a full description of the numerical techniques employed for the simulation of the propeller blade at yaw can be found [14]. The same CFD techniques and grids are employed here. This includes the use of the chimera grid method [31] which allows for overlapping non-matching sub-domains to be defined. The exchange of information between each sub-domain is then achieved through interpolation. As per the previous study, this investigation includes the propeller blades and a fictitious elliptical hub as the foreground grids, with these placed in a sufficiently sized cylindrical background domain. This full domain is presented in Fig. 2.

The blade foreground grid is presented in Fig. 3. To reduce blocking complexity, the blade was cut at the 20% radial posi-

tion. This removes the need for a detailed grid around the blade cylindrical section where hub mounting structures are located. In addition to this, the inflow measurements during the experiment start from the 20% radial station, therefore no data is available for comparison below 20% radius. A radial slice of the foreground mesh can be seen in Fig. 3(b), where the number of grid points around the 60%R aerofoil section is detailed. The normal edges to the aerofoil section are clustered towards the blade, using a hyperbolic law, to a spacing of $1 \times 10^{-5} c_{ref}$. A total of 29 nodes are used to distribute the cells normal to the aerofoil towards the chimera boundary, with a total of 110 cells distributed around the blade section. An O-grid topology was used for the blade foreground as this allowed for the even distribution of blocks around the blade tip and blunt trailing edge. A total of 184 nodes are distributed along the blade radius, clustering towards the tip and root. Overall, the total baseline grid size of the blade foreground is 606,400 cells.

As previously stated, an approximate computational hub was included as a foreground level for the CFD simulations. This was included to obtain some of the blockage effects associated with the experimental hub. In the two-bladed investigation [14], the computational hub geometry is derived using the leading edge curva-

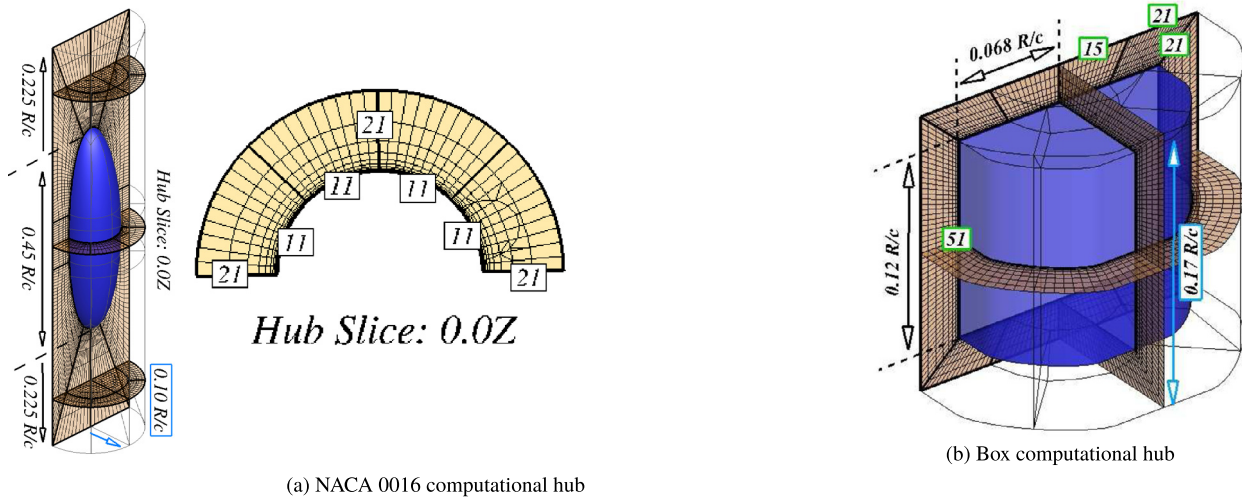


Fig. 4. Fictitious computational hubs included as a foreground mesh.

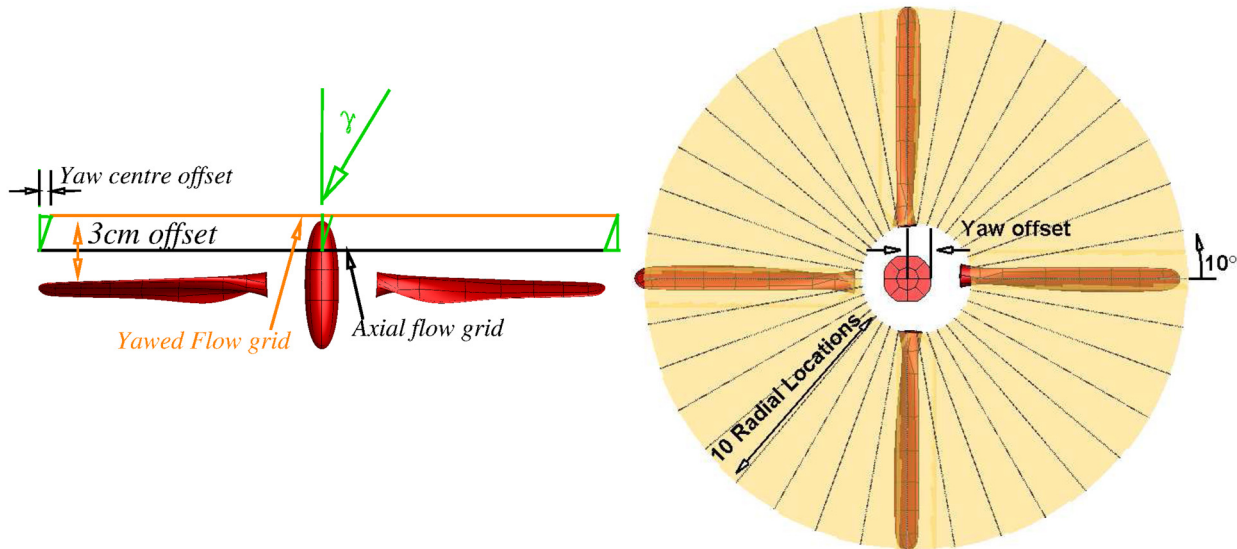


Fig. 5. Inflow grid location and resolution for the yawed flow test case.

ture of the NACA 0016 for the fore and aft components, combined with a cylindrical centre station to provide a total axial length of 0.45 R/c . This is shown in Fig. 4(a) with the blocking topology. In addition to the NACA 0016 hub, a box-shaped hub was built to provide a closer comparison to the experimental setup and this is shown in Fig. 4(b). Due to the increased width of the hub foreground grid, the length is reduced by more than 80%. For both hubs, an O-grid blocking topology is used with all normal edges clustering to $1 \times 10^{-5} c_{ref}$ as per the blade foreground. The full (mirrored) grid size for the NACA 0016 grid is 1,331,200 cells, with 219,520 cells for the box hub.

For the background grid, a standard cylindrical blocking structure is used. To ensure the same level of interpolation between the blade foreground and background, a uniform number of tangential cells are used around the azimuth. This results in a baseline background grid of 19,964,000 cells, for the entire domain. Based upon past experience, grids of this size should be adequate to capture the key flow features.

In line with the experimental study, the extracted inflow plane is at 3 cm upstream of the propeller disc with the same resolution along the radius and azimuth chosen. Due to the offset in freestream velocity, the centre of the inflow plane was adjusted

with this highlighted in Fig. 5. This remains for the compared 3 cm inflow disc, and the subsequent extractions at 2 cm and 1 cm upstream, and 3 cm, 2 cm and 1 cm downstream of the disc.

For the 4-bladed simulations, a combination of the standard Unsteady Reynolds-Averaged Navier-Stokes (URANS), closed using the $k-\omega$ turbulence model [32], and the Scale-Adaptive Simulation (SAS) [33] formulations are used. The SAS model is a hybrid URANS-Large Eddy Simulation method used to introduce elements of the resolved flow. For the SAS formulation, an additional source term is added to the $k-\omega$ Shear Stress Transport (SST) [34] equations which allows for the local adjustment of the von-Karman length scale and balances the contributions from resolved and statistical components. The SAS formulation in HMB3 has been used in the past for transonic cavity flows [35], missile projection [36] and stall flutter predictions [37,38].

2.3. Crigler

In addition to the CFD calculations, the low-order method of Crigler and Gilman [20,39] is used for comparison. In 1944 [39], Crigler published an experimental comparison between existing theory and experimental data. The method used comprised of a blade element theory approach based on a combination of the pro-

propeller axial theory presented by Lock and Yeatman [40] and correction factors obtained from Goldstein [41]. This led to the publishing of the mathematical model in 1952 [20]. The main focus of the model was the assessment of the applicability of available oscillating aerofoil theory to the problem of propellers at incidence. The method relied on the discretisation of the blade and application of steady-state condition assumptions, i.e., calculating the aerodynamic environment for the whole propeller at several azimuthal positions where each iteration uses its local azimuthal location conditions as global for the propeller and consequently averaging out the sum of all of the results. This would still imply forcing a uniform inflow through the whole of the propeller disc, which consequently implies uniform thrust and torque distributions for all propeller blades.

The mathematical representation of the Crigler and Gilman model begins with the calculation of the resultant angle of attack ($\alpha_R(r, \psi)$) and velocity ($V_R(r, \psi)$) around the azimuth (ψ):

$$V_R(r, \psi) = \sqrt{V_T^2 + V_N^2}, \alpha_R(r, \psi) = \beta(r) - \tan^{-1} \frac{V_T}{V_N}, \quad (1)$$

where V_T is the tangential velocity component, V_N is the normal velocity component and β is the blade pitch angle experienced at a given radial (r) and azimuthal position (ψ). These are consequently recast in terms of a first order Fourier function:

$$\begin{aligned} \alpha_R &= \overline{\alpha_R} + \alpha_{Rc} \cdot \cos \psi + \alpha_{Rs} \cdot \sin \psi, \\ V_R &= \overline{V_R} + V_{Rc} \cdot \cos \psi + V_{Rs} \cdot \sin \psi, \end{aligned} \quad (2)$$

where subscripts c and s are the first order Fourier coefficients for the resultant angle of attack and velocity. The results are fed into a function to determine blade loads, in terms of sectional lift (dC_l) and drag (dC_d), as a function of angle of attack and resultant velocity leading to the following distribution, with a lift-curve slope of 2π used for the aerofoils:

$$\begin{aligned} dC_l &= \overline{dC_l} + dC_{lc} \cdot \cos \psi + dC_{ls} \cdot \sin \psi, \\ dC_d &= \overline{dC_d} + dC_{dc} \cdot \cos \psi + dC_{ds} \cdot \sin \psi. \end{aligned} \quad (3)$$

The Fourier formulation of load allows the computation of bound vortex strength via the Kutta-Joukowski theorem [42] as follows:

$$\begin{aligned} \gamma_{bnd} &= \frac{1}{2} \cdot c \cdot [\overline{V_R} + V_{Rc} \cdot \cos \psi + V_{Rs} \cdot \sin \psi] \\ &\cdot [\overline{dC_l} + dC_{lc} \cdot \cos \psi + dC_{ls} \cdot \sin \psi], \end{aligned} \quad (4)$$

where γ_{bnd} is the bound vortex strength and c is the chord length. This is consequently translated to the trailed (γ_t) and shed vorticity (γ_s) strength via the Kelvin-Helmholtz [43] theorems:

$$\gamma_t = \frac{d\gamma_{bnd}}{dr}, \gamma_s = -\frac{d\gamma_{bnd}}{d\psi}. \quad (5)$$

Expanded, the shed vortex strength is defined as:

$$\begin{aligned} \gamma_s &= -\frac{1}{2} \cdot c \cdot [\overline{V_R} + V_{Rc} \cdot \cos \psi + V_{Rs} \cdot \sin \psi] \\ &\cdot (dC_{ls} \cdot \cos \psi - dC_{lc} \cdot \sin \psi) \dots \\ &+ (\overline{dC_l} + dC_{lc} \cdot \cos \psi + dC_{ls} \cdot \sin \psi) \\ &\cdot (V_{Rs} \cdot \cos \psi - V_{Rc} \cdot \sin \psi), \end{aligned} \quad (6)$$

with the trailed vorticity given by:

$$\gamma_t(i) = \gamma_{bnd}(i) - \gamma_{bnd}(i-1) \quad (7)$$

Table 2
Propeller Thrust comparison.

Data source	Force	% Discrepancy
Experimental	15.53 N	-
URANS, $\beta_{0.7R} = 49^\circ$, NACA 0016 Hub	21.83 N	+40.5 %
SAS, $\beta_{0.7R} = 49^\circ$, NACA 0016 Hub	20.05 N	+29.1 %
SAS, $\beta_{0.7R} = 44^\circ$, NACA 0016 Hub	17.06 N	+9.8 %
SAS, $\beta_{0.7R} = 44^\circ$, Box Hub	16.28 N	+4.8 %
Crigler, $\beta_{0.7R} = 49^\circ$	40.37 N	+160 %
Crigler, $\beta_{0.7R} = 40^\circ$	15.42 N	-0.7 %

where i is a counter along the radial positions of the blade. This blade load model is consequently coupled with a semi-rigid wake model with geometry defined by wake age ($\epsilon = -\psi$) as follows:

$$\begin{bmatrix} x_w \\ y_w \\ z_w \end{bmatrix} = \begin{bmatrix} \cos \epsilon + V_p \cdot \frac{\epsilon}{\omega} \\ \sin \epsilon \\ V_n \cdot \frac{\epsilon}{\omega} + v_i(r, \psi) \end{bmatrix} \quad (8)$$

where x_w, y_w, z_w is the wake position, V_p is the in-plane velocity, ω is the blade rotational velocity and v_i the induced velocity. The matrix dictates the location of the wake nodes that are interconnected by straight vortex filaments. The shed and trailed circulation are contained in filaments parallel and normal to the bound vorticity. The wake is extended to five wake rotations. Once the wake is constructed, the induced velocity can be calculated via Biot-Savart law [44]:

$$\vec{v}_i = \sum_{b=1}^B [\vec{v}_{\gamma_t}|_b + \vec{v}_{\gamma_s}|_b] + \sum_{b=2}^B \vec{v}_{\gamma_{bnd}}|_b \quad (9)$$

The wake strength map is set up as a 4D array of size $[ni, nj, B, 3]$ where ni represents the number of radial nodes, nj the number of azimuthal nodes across the wake, B is the number of propeller blades and the last array dimension represents the three spatial dimensions. This allows for the influence of the wake to be calculated as a single matrix operation significantly increasing the computational efficiency of the model.

3. Results and discussion

3.1. Validation work

3.1.1. Blade loading

Before a transition is made to study the aerodynamic profile, a validation process is conducted on the 4-bladed inflow test case. Unlike the previous experimental investigation [13], load cell data is available and, therefore, an effort is made to match this experimental result of 15.53 N. Presented in Fig. 6 is the numerical full propeller and individual blade thrust results. Using the standard pitch presented in Table 1, the average propeller thrust values for both the CFD with URANS and the Crigler method over-estimate the experimental loads with differences of 29.1% and 160%, respectively. The exact load values are presented in Table 2. This over-estimation could be a result of several factors including a discrepancy between the geometries, particularly for the CFD simulation, and the level of modelling. A clear benefit is found when using URANS compared to Crigler in terms of accuracy to the load value. However, the differences between the CFD and experiment themselves was too high and therefore further analysis was conducted in both models looking at the blade pitch angle and the level of turbulence modelling for the CFD.

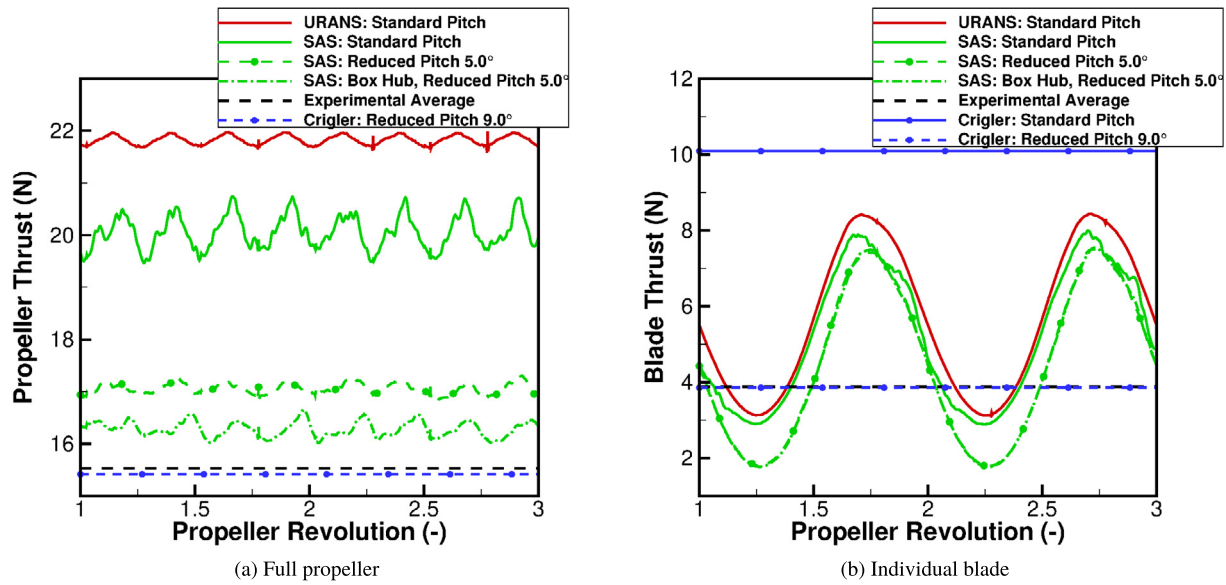


Fig. 6. Numerical propeller and individual blade thrust comparisons.

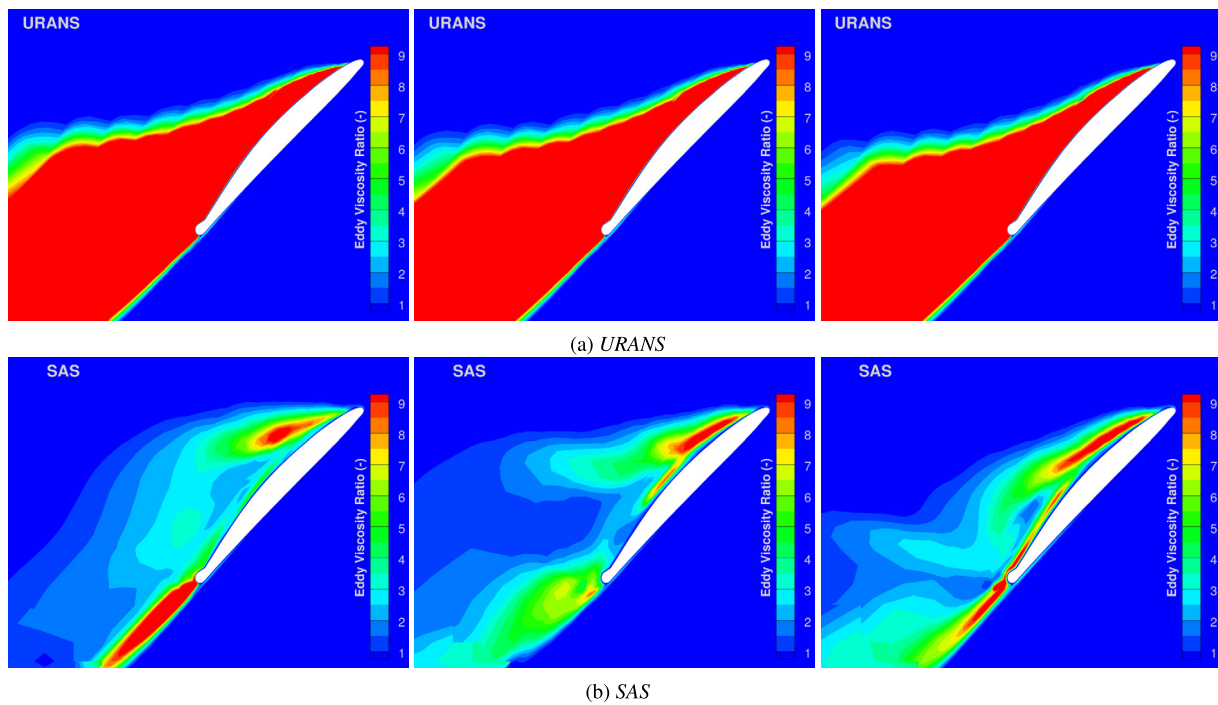


Fig. 7. Eddy viscosity ratio profiles across the 80%R radial station for the URANS and SAS calculations.

In terms of the Crigler method, the pitch angle had to be reduced by 9° to match the experimental data. At 40°, the difference in average load is found to be 0.7%. The significant over-estimation of the Crigler method is highlighted in Fig. 6(b) where the individual blade loading is presented. From the experiment, a single blade is seen to produce 3.9 N at the standard pitch, hence the requirement for a reduction. At the reduced pitch, a single blade produced 3.8 N as estimated by the Crigler method.

For the CFD, the blade pitch was reduced by 5° and the SAS formulation was used. This is because standard URANS formulations are known to over-estimate the blade airloads during stalled conditions, as a result of the lack of vortex shedding in stall due to excessive eddy viscosity [37,38]. This effect of vortex shedding is

highlighted in Fig. 7 where eddy viscosity ratio profiles are examined across the 80%R station for the standard pitch URANS and SAS calculations, respectively, following the peak in individual blade loading. The standard pitch loading results with SAS are used here to highlight the extent of vortex shedding captured when comparing directly URANS and SAS when at the same high pitch angle.

Examining the URANS result (Fig. 7(a)), the overall profile of the eddy viscosity remains consistent across the blade at peak loading with no significant variation. Such stall bubbles are typical with URANS modelling of detached flows due to the excessive dissipation of the turbulence modelling. This excessive dissipation is cut down by SAS allowing for resolved content to be captured. The eddy viscosity ratio SAS profiles therefore indicate areas of local turbulence and velocity fluctuations. As observed in Fig. 7(b), there

is an initial build-up of stalled flow around the leading edge of the blade. This sheds from the surface before a second vortex begins to develop at the trailing edge.

The combination of these changes, including pitch reduction of 5° and use of SAS places the CFD results within 10% of the experimental value (Table 2). The effect of these changes can also be observed in the individual blade loads. Looking at the URANS results, smooth sinusoidal curves are derived, and this is driven by the effects of the retreating/advancing sides with an inflow angle, with no significant fluctuation caused by shedding. All SAS results indicate a reduction in load around and following the advancing side peak. Despite this increase in fidelity in moving from URANS to SAS, there is no significant increase in computational cost. This is one of the benefits of SAS as it uses the same turbulence transport equations at its core with an additional source term for the resolving effect. Overall, a propeller revolution for both URANS and SAS was found to take ~ 4 days across 144 cores with 4 GB of memory each.

The final major difference between the experimental and CFD setup is the hub. In the experiment, a cube-like hub was used to attach the blades to the motor shaft. With the load cell present within that section, the influence of the hub had to be accounted for. Initial results used the NACA 0016 computational hub presented in Fig. 4(a). This hub provided almost no thrust to the overall surface loads within the simulation due to its streamlined design. Following this, the box hub, presented in Fig. 4(b), was installed in the numerical setup and examined with the SAS model and 5° reduced pitch blades. The change in hub design had no effect on the individual blade loads of Fig. 6(b) and this is due to the cut-out between the hub and blades. An influence on the blade loads could potentially be found with a fully integrated hub-propeller system. However, this would significantly increase the mesh complexity. As observed from Fig. 6(a) and Table 2, the box hub reduces the overall thrust by 5% bringing the estimated value now within 5% of the experiment. A similar percentage value difference in thrust was observed in the 2-bladed numerical study and, hence, it can be concluded that the numerical simulation is converged for the 4-bladed result. For the comparison of the induction factors profiles, this converged simulation of SAS with a 5° pitch reduction and the cube hub was used with the reduced pitch (9°) Crigler result to compare against the experimental data as these numerical results best captured the experimental loading.

3.1.2. Inflow induction factors

Presented in Fig. 8 is the comparison of the axial induction factor between the experiment, CFD (SAS with 5° pitch reduction and cube hub) and Crigler for the thrust at 15° yaw and 4-bladed propeller. Examining the profiles qualitatively, the CFD result was able to capture the experimental axial profile better than the Crigler method due to the azimuthal rotation of the maximum induction. An offset is found in the Crigler method from advancing to retreating blade side. However, the maximum location remains at 180° , with the experiment and CFD at $\sim 150^\circ$. For all induction factors, the change in pitch angle from baseline to reduced value made no significant difference to the overall profile. Simply, the areas of low and high values were increased.

Quantitatively, the CFD result was also found to be closer to the experiment than the Crigler method. An experimental maximum of 0.077 was found with the CFD producing 0.073 and the Crigler method producing 0.126. This equates to an under-estimation of the CFD by 5.2% and an over-estimation of the Crigler method by 64%. For both the CFD and Crigler results, the change in pitch angle affected the maximum value. From standard to reduced pitch, the CFD maximum reduced by 16% from 0.087 with the Crigler reducing by 38% from 0.204. No further reduction in maximum was found with the introduction of the cube hub in the CFD. These

percentage reductions due to pitch angle are found to be less than the overall load reduction (Table 2) with the minimum values and additional velocities also having an effect from the freestream yaw.

Due to this over-shoot of the maximum value, the area of the low/negative induction values is found to be significantly higher in the Crigler result compared to the CFD and experiment. Calculating the area of negative induction, the CFD result was found to be 30% higher with the Crigler method 580%. This extension of the negative induction is captured between azimuthal positions 300° and 60° with a radial distance of 0.7R. Both the CFD and experiment remain within 0.4R. For the experimental profile, the minimum value was located at an azimuthal location of $\sim 330^\circ$. A difference is found in the CFD with an azimuthal location of $\sim 90^\circ$. This indicates a greater influence of the box-hub wake. In terms of minimum values, the CFD overshoots this by 21% compared to the experiment with the Crigler result much higher at 102%. For the CFD, the reduction in pitch increased the minimum value magnitude by 47% with a further 205% reduction with the introduction of the cube hub. The Crigler minimum magnitude was found to increase by 24%.

On average, the Crigler method produces a closer axial induction factor to the experiment than the CFD. The average induction values are 0.0289, 0.0301 and 0.0317 for the experiment, Crigler and CFD, respectively. This equates to a 4.2% and 9.7% difference between the Crigler and CFD, respectively, to the experiment. This is expected as the blade loading discrepancy is lower for the Crigler than for the CFD. However, to achieve this, a greater pitch change was required for the Crigler than the CFD.

Presented in Fig. 9 is the comparison of the radial induction factor between the experiment, CFD and Crigler model for the thrust validated 15° yaw, 4-bladed cases. Qualitatively, similarities are found between all radial profiles. The maximum induction values are all contained towards the root of the blade with negative radial induction towards the tip. For both the experiment and CFD, the positive induction values are contained between the root and 0.6R around the propeller azimuth. The Crigler method only produces a positive radial induction value towards 0.6R between azimuth positions $\sim 45^\circ$ and $\sim 315^\circ$. Outside of this area, the positive radial induction is contained to within 0.3R. In terms of azimuthal area, the CFD is found to be 35% below the experiment with the Crigler result 63%.

Due to this reduction in area, the maximum values for both numerical methods are higher than the experiment. The experiment produced a maximum value of 0.082, with a maximum in the CFD of 0.129 and 0.160 for Crigler. This equates to increases of 57% and 95% for the CFD and Crigler, respectively. Additionally, the position of the maximum finds a closer correlation between the experiment and CFD than the Crigler. As observed, the experiment sees the maximum radial induction around 180° . For the CFD, this is slightly offset around 135° with the Crigler at the opposite side around 0° . Due to the over-prediction of the maximum value, the minimum (negative) induction for the Crigler method is seen to overshoot the experimental value as well with a difference of 95%. For the CFD, the difference to the experiment is much closer with an under-prediction of 7%.

The effect of pitch on the Crigler method is found to have the opposite effect in the radial velocity than the axial, with the maximum value increasing in magnitude by 20% and the minimum decreasing in magnitude by 42%. However, for the CFD, the effect of the pitch reduction is found to be fairly minimal (compared to the axial differences) with a 7% and 9% change in magnitude for the maximum and minimum, respectively. The greatest change for the CFD is driven by the introduction of the cube hub with the maximum value increasing in magnitude by 152% from the 0016 hub. This is likely due to the fact the maximum value is found

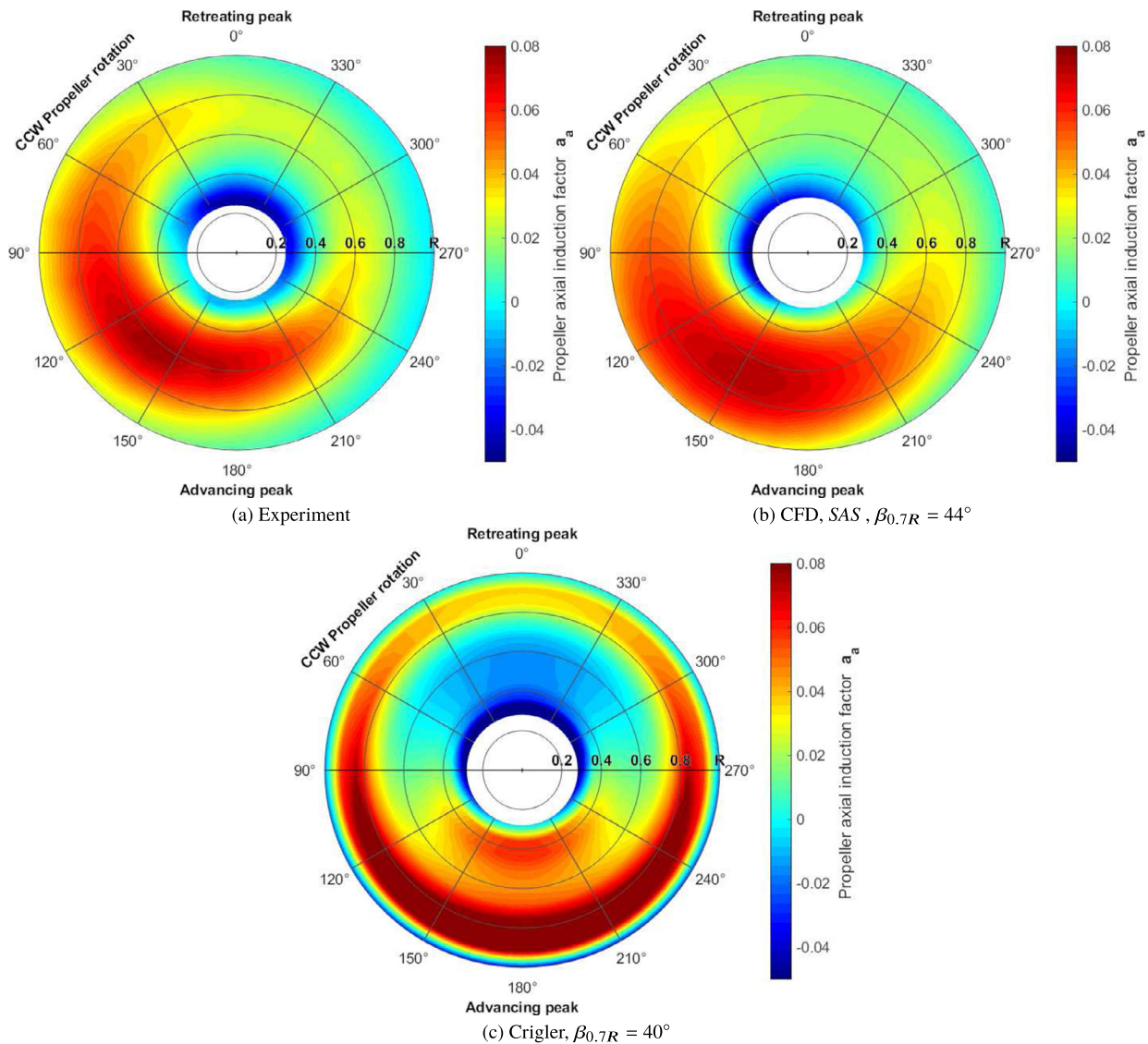


Fig. 8. Comparison of the experiment, CFD and Crigler axial inflow results for the 15° yaw 4-bladed validation case.

close to the blade root, hence the larger influence of the cube hub is captured.

Overall, as per the axial profile, a closer correlation is found between the experiment and CFD results. This is both qualitatively and quantitatively when examining positive and negative induction regions along with the magnitude limits. This closer correlation is also found in the average induction magnitude values with a difference of 5% between the experiment and CFD with the Crigler average 200% larger than the experiment. This is despite the Crigler loading being closer to the experiment and therefore highlights the ability of the CFD to better capture the aerodynamics.

Presented in Fig. 10 is the comparison of the tangential induction factor between the experiment, CFD and Crigler method for the thrust validated 15° yaw, 4-bladed cases. It is the tangential velocity profiles that produce the lowest magnitude induction values of the three profiles. Hence, any small difference is likely to have a large percentage difference. However, looking at the profiles, similarities are found between the sources.

The experiment produces a profile with two distinct peaks in terms of positive and negative induction. The experimental negative induction is found around 240° and extends between 180° and 300° with the radial distance reducing as the profile reaches

300°. A similar result is found for the CFD, however, the radial distance remains more consistent towards 300° before sharply increasing. The Crigler method produces a negative induction bubble between 180° and 255°, however, the average value has a higher magnitude. Looking at the average values within these azimuthal ranges, the CFD is found to under-estimate the experiment by 5.6% with the Crigler over-estimating by 183%.

A similar, and opposite, positive induction bubble is seen in the results around 120° azimuth. The experimental result sees the positive induction range from 315° to 165° (rotating anti-clockwise). Between 0° and 90°, the positive induction is found across the entire blade radius with the bubble shrinking towards the root at 165° and towards the tip at 315°. This creates a maximum value around 135° at the root. A similar profile is found in the CFD result with a maximum around 135°, an entire positive induction value across the radius around 90°, a contraction towards the root at 165° and contraction towards the tip between 30° and 0°. This shrinking towards the tip does not extend to the same azimuthal location as the experiment and hence the full radial positive sweep is reduced. The Crigler method follows the trends of the negative bubble in that the area is significantly reduced with a higher

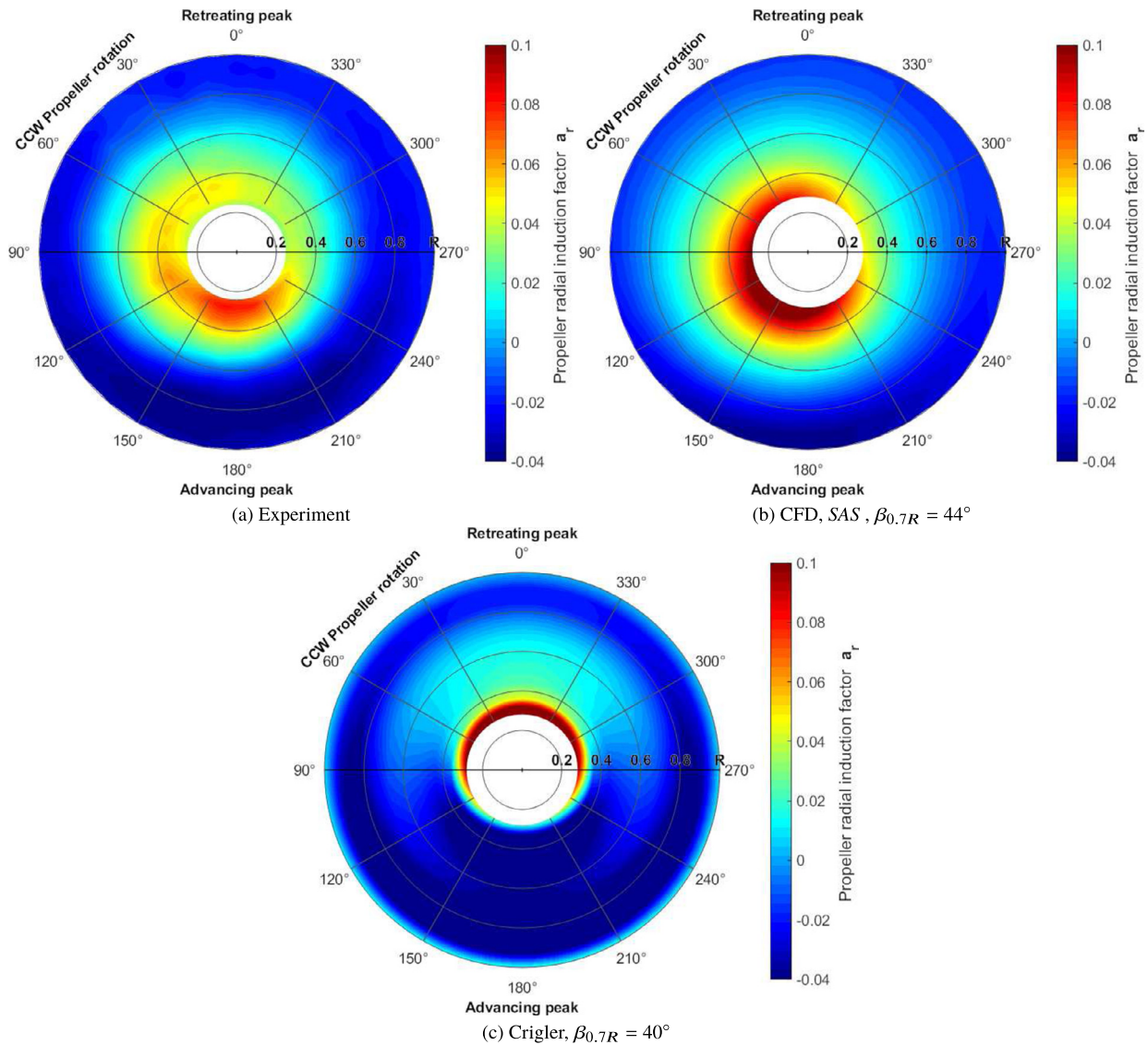


Fig. 9. Comparison of the experiment, CFD and Crigler radial inflow results for the 15° yaw 4-bladed validation case.

overall magnitude. The positive azimuthal range is found to extend from 90° to 165° with no real contraction at either end.

In addition to these two distinct bubbles, the Crigler method produces four additional areas across the retreating side of the blade. Two positive induction bubbles are seen at the tip between 270° and 0° and at the root between 0° and 90°. The opposite is seen for two negative bubbles with a root section between 270° and 0° and tip section between 0° and 90°.

The effect of the pitch on both numerical models is found to have the opposite effect in terms of the magnitudes for both the maximum and minimum. For the Crigler method, the reduction in pitch increased the magnitude of the maximum and minimum by 20% and 10%, respectively. The CFD results finds a decrease in maximum and minimum magnitude by 18% and 13%, respectively, with a reduction in pitch. Like the radial velocity, the introduction of the cube hub to the CFD is found to increase the tangential velocity maximum by 50% with almost no change in minimum.

As a result of these additional bubbles and the higher magnitudes found within them, the average value for the Crigler method is found to have the opposite sign with a value of 0.00019. The CFD and experiment are much closer with values of 0.00023 and 0.00022, respectively. Therefore, in a similar manner to the radial,

the CFD result can capture the aerodynamics of the inflow better than the Crigler method.

3.2. Aerodynamic profile across the 4-blade propeller at yaw

Upon the validation of the yawed test case (SAS with 5° pitch reduction and box hub), the extrapolated computational data, for each velocity profile, is presented below. As previously described, a total of six planes were extracted from 3 cm upstream (the examined inflow plane) to 3 cm downstream of the propeller, with increments of 1 cm. No plane was extracted along the propeller disc, i.e. 0 cm, due to the interference with the blades.

3.2.1. Axial velocity results

Presented in Fig. 11 are the inflow and outflow results for the axial velocity across the propeller disc at yaw. Examining the transition qualitatively it can immediately be discerned that there is a significant change in the behaviour of the inflow and wake. On the inflow side, a singular maximum increasing in magnitude can be observed. Furthermore, it propagates from being approximately one-sixth of the propeller plane to covering half of it as it transitions through the inflow. The maximum tends to remain in the same location radially. Azimuthally, the inflow location tends to

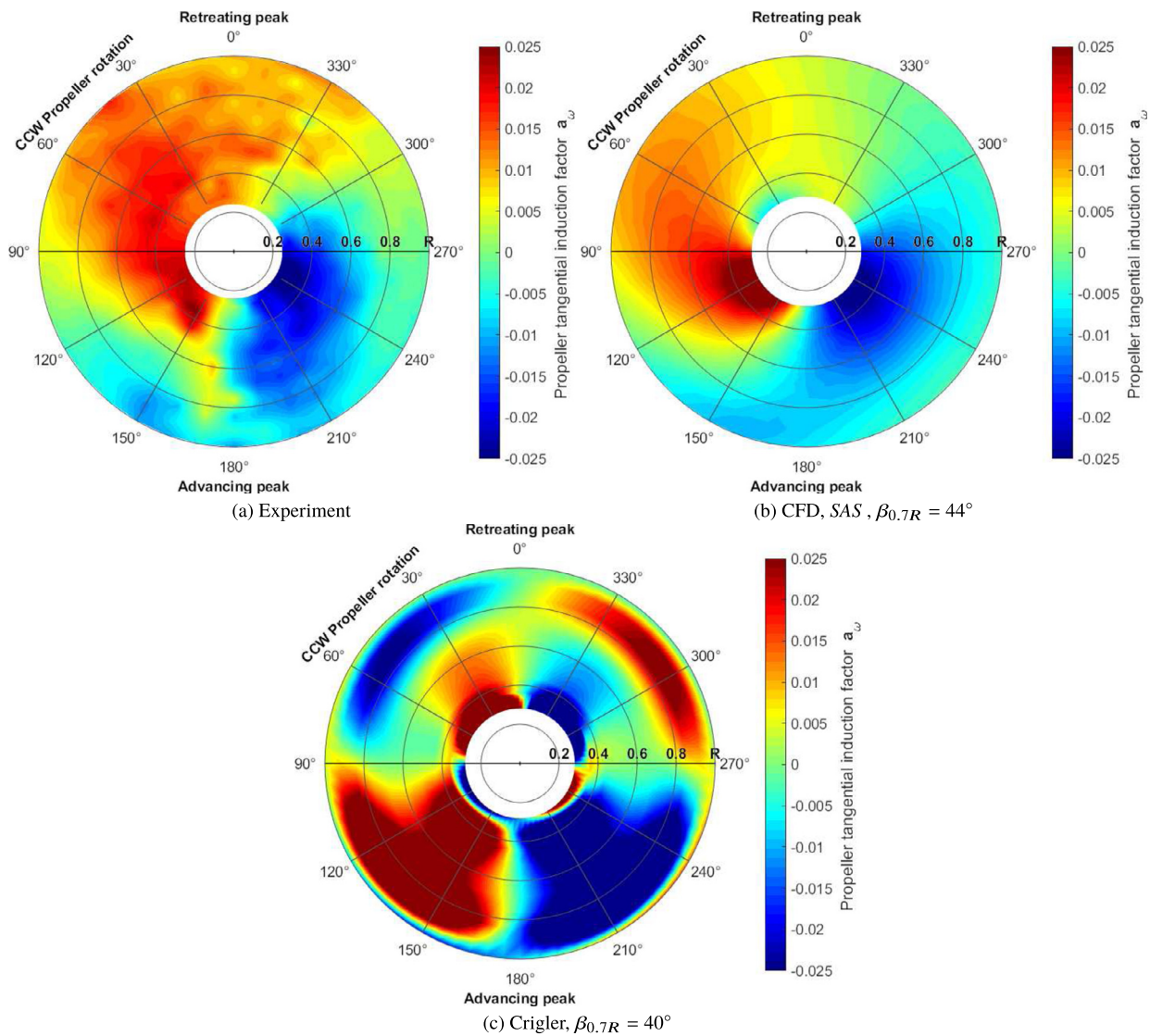


Fig. 10. Comparison of the experiment, CFD and Crigler tangential inflow results for the 15° yaw 4-bladed validation case.

move positively on the azimuth, matching the propeller rotational direction and the swirl velocity generated by it. Overall, the entire propeller field is increasing in magnitude but is doing so by scaling the patterns that exist upstream and their magnitude. Shifting the attention to the root section of the inflow planes it can be seen that the minima region shrinks as the flow accelerates towards the propeller.

Observing beyond the propeller pressure jump - new patterns start to form. Both the maxima and the minima split from singular shapes to having multiple maxima. The aforementioned maxima also develop in terms of shape as they elongate azimuthally and reduce radially. These are speculated results of the interference (constructive and destructive) of the vortical structures generated by the propeller, the largest impact of which is attributed to the propeller tip vortical system. Flow increment is still present in the first two planes of the outflow, with a slight decrease in the retreating blade and central sections of the last outflow plane. The root section downstream of the propeller demonstrates a significant increase in reverse flow magnitude and propagation. This is attributed to a flow re-circulation created by the presence of the propeller hub and the consequent low-pressure field it creates. This is speculated to be exacerbated by the lack of a propeller shaft in the computational domain.

Presented in Table 3 are the maximum and minimum axial induction values, along with the azimuthal positions, for each examined plane. The percentage differences between each plane are also presented. As is seen, the maxima magnitudes across the propeller show an exponential increase as inflow approaches the propeller. The largest increase is between the 2 and 1 cm inflow planes, with a magnitude increase of 37.2%. Once the flow transitions beyond the propeller, where there is a spike in the maxima at 1 cm outflow, the maxima magnitude continues to increase until 2 cm before beginning to fall at 3 cm. The azimuthal position of the maximum increases by ~ 10° from 3 cm to 2 cm inflow. This is then followed by a secondary jump of ~ 10° during the transition between outflow and inflow with a final decrease at 3 cm outflow. The 3 cm inflow and outflow maxima azimuthal positions demonstrate an interesting trend by matching within 10° discrepancy, having the maxima essentially mirroring the inflow and returning to its initial position within the experimental context.

The minimum magnitude is found to decrease during the inflow with the largest change of 40.7% coming as the plane approaches the propeller at 1 cm. This is then followed by a significant increase in magnitude of 121.9% during the transition to outflow before a gradual increase in magnitude at outflow planes 2 cm and 3 cm.

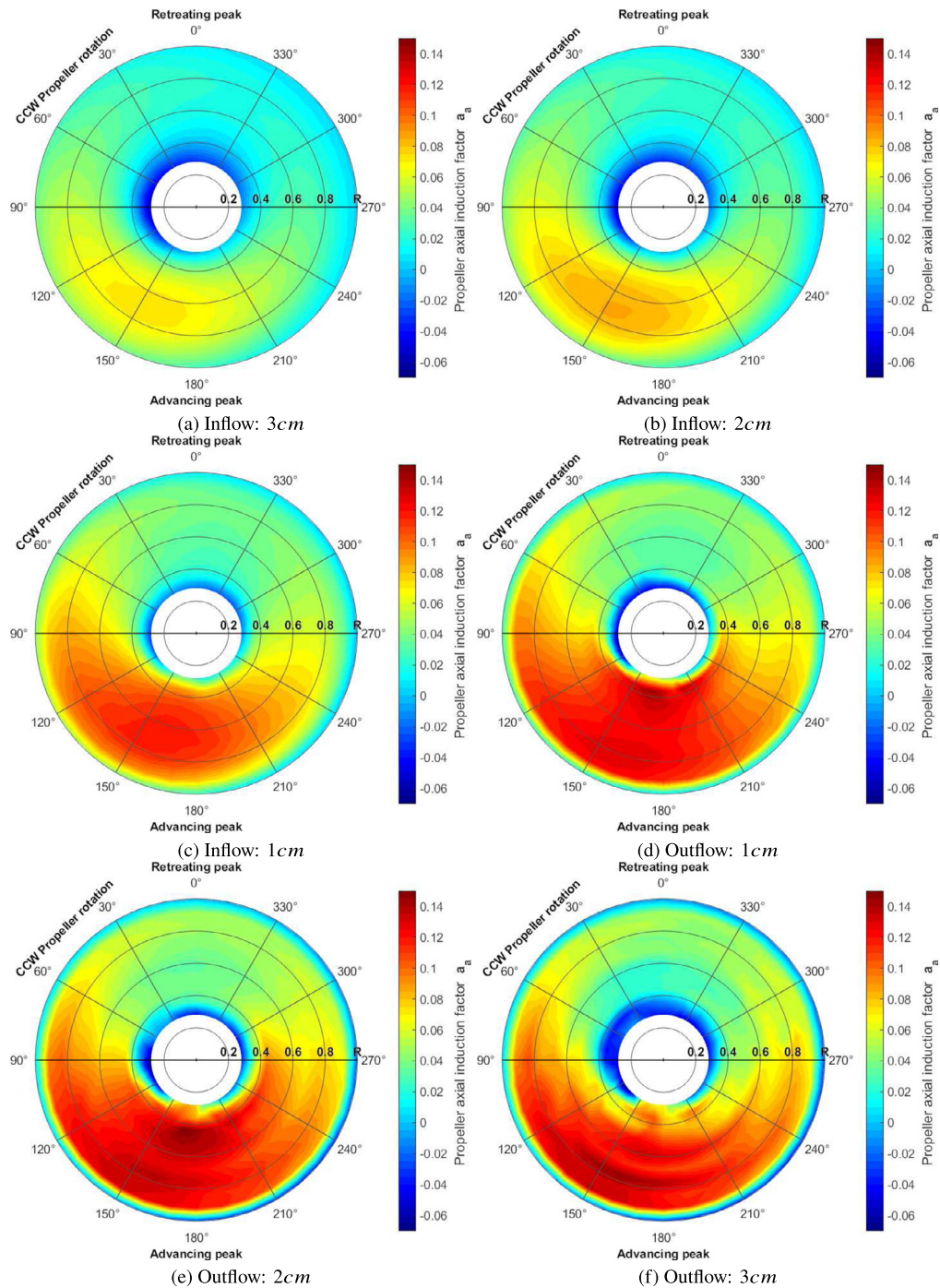


Fig. 11. CFD results of the change in the axial velocity aerodynamic profile through the propeller disc for the 15° yaw test case.

Table 3
Axial induction factor development across propeller inflow and wake.

	Inflow			Wake		
	3 cm	2 cm	1 cm	1 cm	2 cm	3 cm
a_{max} ($\Delta\%$)	0.073 (-)	0.086 (+17.8)	0.118 (+37.2)	0.142 (+20.3)	0.150 (+5.6)	0.145 (-3.3)
a_{av} ($\Delta\%$)	0.031 (-)	0.037 (+19.3)	0.058 (+56.7)	0.068 (+17.2)	0.069 (+1.4)	0.062 (-10.1)
a_{min} ($\Delta\%$)	-0.058 (-)	-0.054 (-6.8)	-0.032 (-40.7)	-0.071 (+121.9)	-0.073 (+2.8)	-0.075 (+2.7)
ψ_{max} (Δ°)	150.0 (-)	160.1 (+10.1)	160.0 (-0.1)	169.7 (+9.7)	170.2 (+0.5)	159.6 (-10.6)
ψ_{min} (Δ°)	84.9(-)	90.8 (+5.9)	91.2 (+0.4)	108.8 (+17.6)	97.3(-11.5)	127.6 (+30.3)

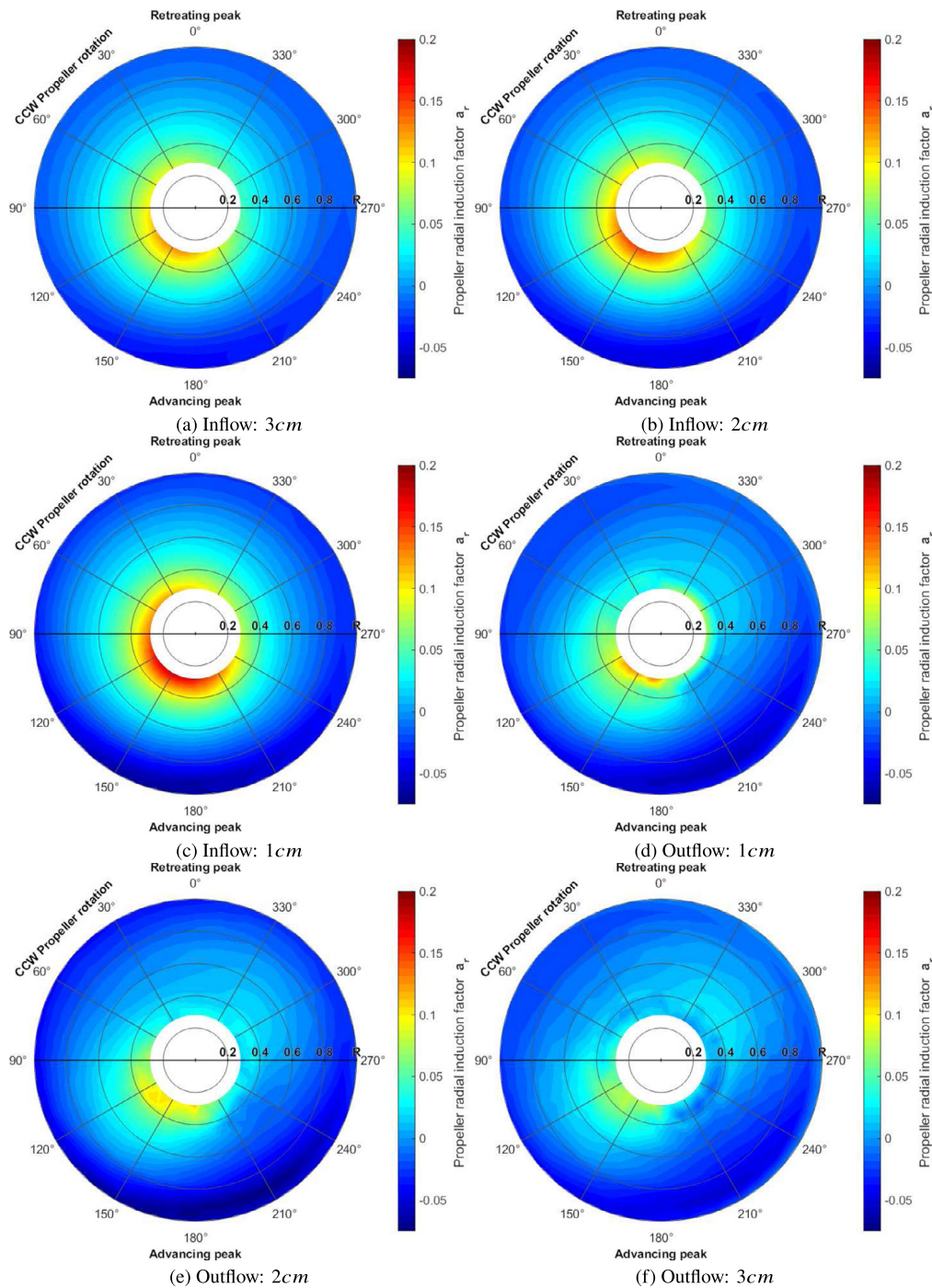


Fig. 12. CFD results of the change in the radial velocity aerodynamic profile through the propeller disc for the 15° yaw test case.

3.2.2. Radial velocity results

Presented in Fig. 12 is the radial velocity profile through the propeller disc when at yaw. Examining the radial induction factors qualitatively across the propeller field demonstrates four behavioural main patterns. The first is the increment of the maxima as the inflow approaches the propeller. The maxima both increase in magnitude and area. This pattern is mainly attributed to the stagnation point generated in the frontal area of the propeller hub.

On the other side of the propeller, a gradual decrease of the maxima can be observed, forming the second pattern. While the decrease is significant, the root section does not reach negative radial velocities within the 3 cm experimental domain. It is speculated that once the imparted flow momentum decreases a re-

circulation with the negative flow in the hub section will be present.

The behaviour of the minima can also be described by two patterns. Firstly, as the inflow approaches the propeller, the amplitude of the tip blade section increases around the whole azimuth without any notable change of the pattern.

Once the pattern transitions over the propeller, an increase in area and intensity diffusion can be observed. Both increases moving away from the propeller plane. It is interesting to note that for the 3 cm outflow the flow pattern in the root regions consists of a dotted structure, possibly suggesting a complex flow interaction.

Quantitatively, as presented in Table 4, the maximum demonstrates an exponential increase pattern approaching the propeller

Table 4
Radial induction factor development across propeller inflow and wake.

	Inflow			Wake		
	3 cm	2 cm	1 cm	1 cm	2 cm	3 cm
a_{max} ($\Delta\%$)	0.129 (-)	0.151 (+17.0)	0.181 (+19.8)	0.131 (-27.6)	0.110 (-16.0)	0.080 (-27.7)
a_{av} ($\Delta\%$)	0.007 (-)	0.008 (+14.3)	0.008 (0)	-0.004 (-150.0)	-0.008 (+100)	-0.005 (-37.5)
a_{min} ($\Delta\%$)	-0.041 (-)	-0.051 (+24.4)	-0.070 (+37.3)	-0.063 (-10.0)	-0.076 (+20.6)	-0.055 (-27.6)
ψ_{max} (Δ°)	146.5 (-)	141.2 (-5.3)	147.7 (+6.5)	168.7 (+21.0)	180.0 (+11.7)	169.6 (-10.4)
ψ_{min} (Δ°)	170.2(-)	170.1 (-0.1)	170.3 (+0.2)	199.7 (+29.4)	203.5 (+3.8)	206.8 (+3.3)

with a 17.0% and 19.8% increase between the inflow stations. The transition from inflow to wake shows a 27.6% decrease in maxima followed by a further exponential decrease in the wake.

In terms of azimuthal location, the maximum shows a minimal change in peak position across the planes, except for the propeller plane transition. It contains a 21.0° azimuthal shift with the wake radial maxima leading.

While the behaviour of the minima demonstrates a similar exponential increase pattern in the inflow, it does show an interesting pattern within the wake. The propeller transition marks a 10% decrease, which suggests interference between the wake tip vortices. Further downstream, the minima continue to increase in magnitude (20.6%) between the first two positions. The last transition is decremental in magnitude (27.6%), owed predominantly to tip vortex cross interaction.

The radial azimuthal minimum position exhibits almost no changes between the first two inflow positions, with a 29.4° shift during the propeller transition. All other transitions demonstrate an approximately linear lagging in position while moving downstream.

3.2.3. Tangential velocity results

Presented in Fig. 13 is the tangential velocity profile through the propeller disc when at yaw. Looking at the tangential inflow factor sequence some interesting results can be discerned. The pattern starts off with two distinct extrema, with similar shape, opposing magnitude and each contained within approximately half of the propeller disc. The maxima of both patterns are located in the blade root region and interestingly not on opposite azimuthal positions. The positive extrema are located at the 120° location while the negative one is around the 250° azimuth. Both patterns have their radial extrema lagging as the pattern moves towards the tip of the propeller.

With the transition from inflow to wake, a significant increase in tangential velocity is present reflecting the swirl velocity imparted by the propeller on the wake. The maxima and minima patterns within the wake are now reallocated in azimuthally opposite locations slightly lagging behind the advancing and retreating peaks. As the pattern advances within the wake its azimuthal location remains consistent, however, the extrema structures change. The maxima, located around the 170° azimuthal location tends to increase in area and amplitude between the first and second wake positions. This is followed by a further increase in the area coupled with a diffusion of the amplitude. The maxima in the last position are split into three distinct maxima which can be speculated to be tied to wake interactions. The minimum in an opposite manner shows a reduction in the area as it concentrates around the root section on the retreating half of the propeller plane.

From a quantitative standpoint on the inflow side (Table 5), the approach demonstrates an initial 20.5% increase in maxima magnitude before levelling off, where the latter could be speculated to be a result of the discussed above reduction pattern. The most significant transition as expected is the jump from inflow to wake,

bearing an increase of maxima magnitude of 260.7%. Consequent wake behaviour bears a quadratic response with an initial increase in maxima magnitude of 7% at 2 cm followed by a returning decrease of 7% at 3 cm. In terms of position, the most significant transition is again the one through the propeller, with the wake leading the inflow by 31.1°. This is followed by a return to a similar position as the inflow with a return shift in azimuth position of 39.9°.

In terms of minima, an exponential increase in magnitude (13.8 and 45.5%) can be observed approaching the propeller field. The propeller transition results in the only decrease in minima magnitude with a shift of 87.5%. This is then followed by a decreasing increase in magnitude at 2 cm and 3 cm outflow of 66.6% and 20.0%, respectively. In terms of azimuthal position, an overall increase is found during the inflow from 3 cm to 1 cm, with a small decrease of 2.2° at 2 cm. Hence, the greatest shift during the inflow is found between 2 cm and 1 cm. After the transition, the wake minima location exponentially lags through the wake at 2 cm and 3 cm. The transition through the propeller again demonstrates the largest shift in azimuthal position confirming the qualitative observations with 80.1°.

While experiments were conducted for the 3 cm inflow case at higher test point density, it is not certain that as the flow moves through the propeller more small scale behaviour could develop. As such, it might be of interest to use a higher resolution test probe plane for the wake sections of the results, to ensure no part of the pattern is limited by the current resolution. This pertains to all three induction factors discussed.

4. Conclusions

The following conclusions are observed from the validation procedure:

Differences were found between the blade loading of the CFD and the experiment. As a result, an examination of the turbulence modelling, blade pitch angle and hub geometry are conducted. The use of SAS with a 5° pitch change and the use of a hub that better matches the experimental setup resulted in a closer result to the experiment. The use of SAS indicates that the blade was in the presence of stall for a portion of the rotation. Hence, improved modelling was required to capture the vortex shedding. Combining these changes resulted in a load agreement of within 5%. Likewise, the Crigler method was used to compare with the CFD and experimental data in terms of blade loading and inflow profiles. A similar over-estimation of the loads was achieved with the method in reference conditions and as such a pitch reduction was required to match the loading. A higher change was required in the Crigler method compared to the CFD with a reduction of 9°.

Similarities were found in the inflow profiles between the numerical and experimental results for all velocities. Aside from the average axial induction value, a closer agreement was found between the CFD and experiment than Crigler. Additionally, the CFD was

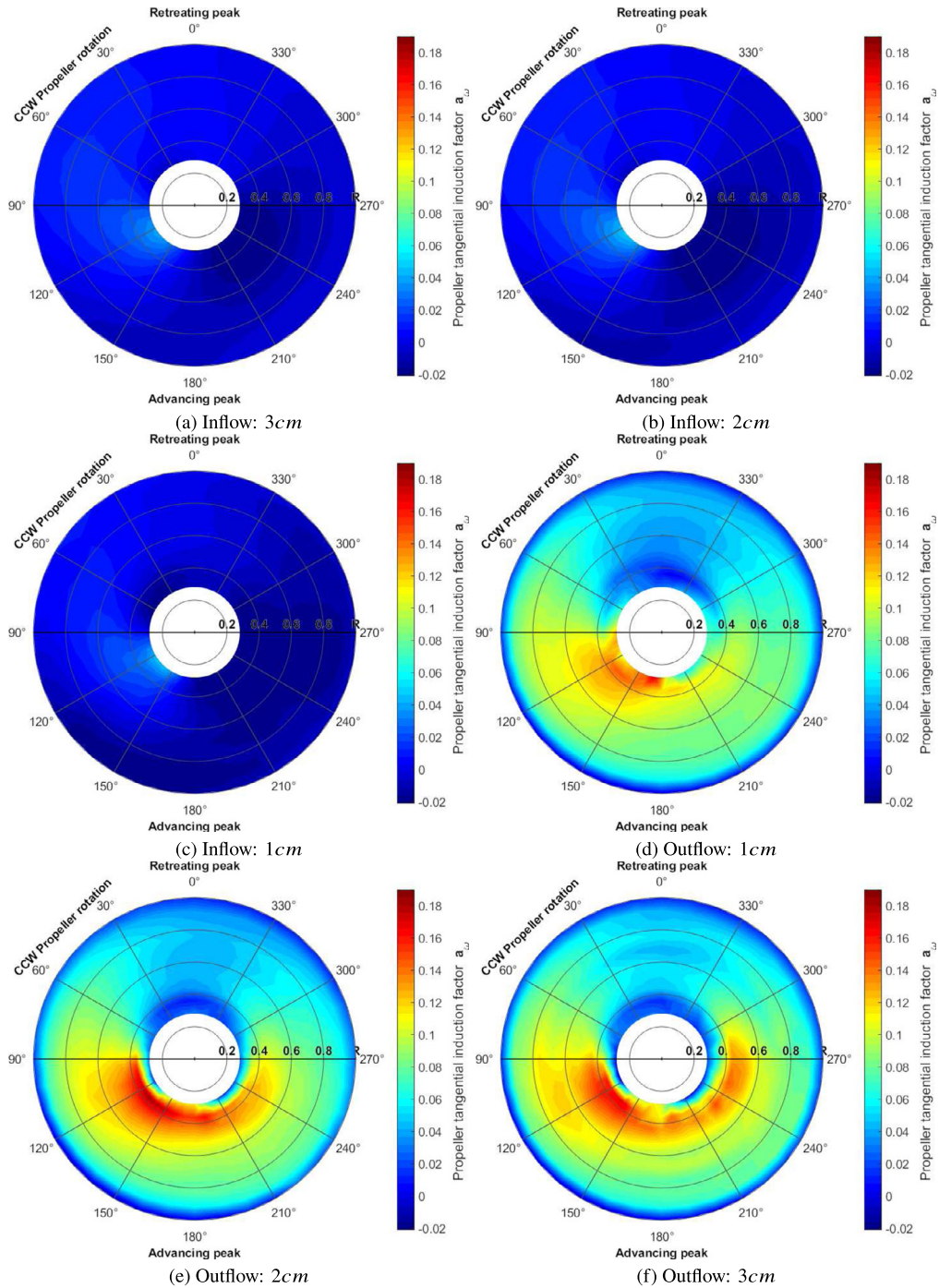


Fig. 13. CFD results of the change in the tangential velocity aerodynamic profile through the propeller disc for the 15° yaw test case.

Table 5
Tangential induction factor development across propeller inflow and wake.

	Inflow			Wake		
	3 cm	2 cm	1 cm	1 cm	2 cm	3 cm
a_{max} ($\Delta\%$)	0.039 (-)	0.047 (+20.5)	0.047 (0)	0.170 (+260.7)	0.182 (+7.0)	0.169 (-7.1)
a_{av} ($\Delta\%$)	0.000 (-)	-0.001 (0)	-0.007 (-600)	0.068 (+1071.4)	0.071 (+4.4)	0.075 (+5.6)
a_{min} ($\Delta\%$)	-0.029 (-)	-0.033 (+13.8)	-0.048 (+45.5)	-0.006 (-87.5)	-0.010 (+66.6)	-0.012 (+20.0)
ψ_{max} (Δ°)	129.2 (-)	129.7 (+0.5)	138.8 (+9.1)	169.9 (+31.1)	130.6 (-39.9)	139.4 (+8.8)
ψ_{min} (Δ°)	232.9 (-)	230.7 (-2.2)	240.2 (+9.5)	160.1* (-80.1)	147.9* (-12.2)	110.9 (-37)
	-	-	-	351.1* (+111.1)	9.6* (+18.5)	-

* Secondary minima of interest located inboard (Primary is located at blade tip).

able to capture better some of the intricate details of the profiles that Crigler could not. This includes the offset of the maximum axial induction, the radial extent of the radial induction and the positioning of the positive and negative tangential induction bubbles.

Based upon the agreement in blade loading and the inflow profiles, the agreement was deemed close to allow for further analysis of the aerodynamic profile through the disc plane. The following conclusions of these are as follows:

For both the axial and radial velocities, the profiles remain consistent between the inflow and outflow regions. Only small changes in magnitude and extreme locations are captured between each plane with often the greatest shift found during the transition. The tangential profile sees the greatest change in profile and magnitude from the inflow to outflow regions. This is due to the influence of the swirl velocity within the propeller wake.

Both maxima and minima axial trends during the inflow to the propeller are found to exponentially shift in magnitude with an increasing trend for the maxima and decreasing trend for the minima. The transition from inflow to outflow results in an increase in magnitude for both extremes, with the maxima quadratically shifting from 1 cm to 3 cm outflow and the minima following a stable increase in magnitude. The location of the axial maxima follows an interesting trend in both outflow and inflow where no change is found between the 1 cm and 2 cm planes and $\sim 10^\circ$ changes from 3 cm to 2 cm at the inflow and 2 cm to 3 cm at the outflow. The axial minima follows a similar trend during the inflow, with no change between 2 cm and 1 cm. In the wake, there is an initial increase due to the transition before decreasing at 2 cm and then increasing to the largest azimuthal value at 3 cm.

A similar exponential trend is exhibited by the radial induction factor maxima and minima with increasing magnitudes during the inflow. Unlike the axial maxima where there is an initial increase in magnitude in the wake, the radial maxima decreases due to the transition and continues to decrease in magnitude into the wake. The minima follows a quadratic response with a peak in magnitude a 2 cm. The locations of the maxima and minima see a varying response during the inflow, with the minima fairly consistent and the maxima decreasing before increasing again as it approaches the propeller. The greatest change in location for both extremes are observed at the transition point with similar increases of $> 20^\circ$. The increase in minima location is continued into the wake until the 3 cm plane with the maxima location falling off at 3 cm.

The tangential maxima and minima are found to increase in magnitude as they approach the propeller. The maxima reaches its peak earlier at 2 cm with the minima inflow peak occurring at 1 cm. The transition to outflow results in a significant increase in maxima magnitude and decrease in minima magnitude. After the transition, the minima magnitude begins to increase in magnitude, however still lower than the inflow values. The maxima, like the radial and axial, initially increases at 2 cm before starting to dissipate at 3 cm outflow. The locations of the extremes remain consistent during the inflow up until 1 cm, where a $\sim 10^\circ$ increase occurs. The transition results in a significant shift in location with the minima splitting into two distinct peaks. This secondary peak continues until 2 cm before dissipating at 1 cm. The maxima location in the wake increase in value immediately after the transition before correcting at 2 cm and then returning to a similar 1 cm inflow value at the 3 cm outflow stage.

Overall, the formation of extrema with an azimuthal shift from the advancing and retreating peaks is consistent across all cases. Furthermore, all major thrust generation related patterns within the flow tend to follow similar behaviour as they travel through the control volume, defining the influence in yaw on the system.

Declaration of competing interest

The authors declare that they have no known competing financial interests or personal relationships that could have appeared to influence the work reported in this paper.

Acknowledgements

This work used the Cirrus UK National Tier-2 HPC Service at EPCC (<https://www.epcc.ed.ac.uk/cirrus>) funded by the University of Edinburgh and EPSRC (EP/P020267/1) under project number EC004. Results were obtained using the ARCHIE-WeSt High Performance Computer (<http://www.archie-west.ac.uk/>) based at the University of Strathclyde.

The support provided by the Engineering and Physical Sciences Research Council (EPSRC), the Aircraft Research Association (ARA), the National Wind Tunnel Facility (NWTF) of the United Kingdom, and the U.K. Vertical Lift Network (UKVLN) is gratefully acknowledged.

References

- [1] F. Bramwell, E. Relf, L. Bryant, Experiments on Model Propellers at the National Physical Laboratory, (ii) Experiments to Determine the Lateral Force on a Propeller in a Side Wind, British ACA, 1914.
- [2] W. Durand, E. Lesley, Tests on air propellers in yaw, NACA TR 113, 1923, <https://ntrs.nasa.gov/search.jsp?R=19930091176>.
- [3] O. Flachsbar, G. Krober, Experimental investigation of aircraft propellers exposed to oblique air currents, NACA TM 562, 1930, <https://ntrs.nasa.gov/search.jsp?R=19930094852>.
- [4] H.B. Freeman, The effect of small angles of Yaw and Pitch on the characteristics of airplane propellers, NACA TR 389, 1932, <https://ntrs.nasa.gov/search.jsp?R=19930091463>.
- [5] R. Harris, Forces on propeller due to sideslip, Technical Report, British Aeronautical Research Council, 1918.
- [6] E. Lesley, G. Worley, S. Moy, Air propellers in yaw, NACA TR 597, 1937, <https://ntrs.nasa.gov/search.jsp?R=19930091672>.
- [7] W. Gray, J. Hallissy, A. Heath, A Wind-Tunnel Investigation of the Effects of Thrust-Axis Inclination on Propeller First-Order Vibration, NACA TR 1205, 1954, <https://ntrs.nasa.gov/search.jsp?R=19930092216>.
- [8] R. Pendley, Effect of propeller-axis angle of attack on thrust distribution over the propeller disk in relation to wake-survey measurement of thrust, J. Appl. Phys. 14 (8) (1943) 399, <https://doi.org/10.1063/1.1715007>.
- [9] H. McLemore, M. Cannon, Aerodynamic investigation of a four-bladed propeller operating through an angle-of-attack range from 0 to 180 degrees, NACA TN 3228, 1954, <https://ntrs.nasa.gov/search.jsp?R=19930084170>.
- [10] J. Russell, Wake Survey and Strain-Gauge Measurements on an Inclined Propeller in the RAE t 24-ft Tunnel Parts I and II, Report N 648, Aeronautical Research Council, 1953, <https://ntrs.nasa.gov/search.jsp?R=19930090927>.
- [11] J. Russell, Wake survey and strain-gauge measurements on an inclined propeller in the r.a.e. 24-ft tunnel: Part 2: Strain-gauge measurements, Tech. Rep. 648, British Aeronautical Research Council, 1953.
- [12] P. Yaggi, V. Rogallo, A wind-tunnel investigation of three propellers through an angle of attack from 0 to 85, NASA TN D-318, 1960, <https://ntrs.nasa.gov/search.jsp?R=19890068078>.
- [13] A. Zarev, R. Green, Experimental investigation of a two-bladed propeller at incidence, Aersp. Sci. Technol. 103 (2020), <https://doi.org/10.1016/j.ast.2020.105940>.
- [14] R.J. Higgins, A. Zarev, G.N. Barakos, R.B. Green, Numerical investigation of a two-bladed propeller inflow at yaw, J. Aircr. (2019), <https://doi.org/10.2514/1.C035647>.
- [15] G. Chirico, G. Barakos, N. Bown, Numerical aeroacoustic analysis of propeller designs, Aeronaut. J. 122 (1248) (2018) 283–315, <https://doi.org/10.1017/aer.2017.123>.
- [16] R. Steijl, G.N. Barakos, K. Badcock, A framework for cfd analysis of helicopter rotors in hover and forward flight, Int. J. Numer. Methods Fluids 51 (8) (2006) 819–847, <https://doi.org/10.1002/flid.1086>.
- [17] V. Leble, G. Barakos, Demonstration of a coupled floating offshore wind turbine analysis with high-fidelity methods, J. Fluids Struct. 62 (2016) 272–293, <https://doi.org/10.1016/j.jfluidstructs.2016.02.001>.
- [18] S. Shahpar, SOPHY: an integrated CFD based automatic design optimisation system, in: International Symposium on Air Breathing Engines, American Institute of Aeronautics and Astronautics, Munich, Germany, ISBN 9781563477904, 2005.
- [19] J. De Young, Propeller at high incidence, J. Aircr. 2 (3) (1965) 241–250, <https://doi.org/10.2514/3.43646>.

- [20] J. Crigler, J. Gilman, Calculation of aerodynamic forces on a propeller in pitch or yaw, *Technical Note 2585, National Advisory Committee for Aeronautics*, 1952.
- [21] D.M. Pitt, Rotor dynamic inflow derivatives and time constants from various inflow models, Army troop support and aviation material readiness command, St Louis, MO, 1980, <https://apps.dtic.mil/docs/citations/ADA099532>.
- [22] D.A. Peters, N. HaQuang, Dynamic inflow for practical applications, *J. Am. Helicopter Soc. (ISSN 0002-8711)* 33 (1988) 64–68, <https://ntrs.nasa.gov/search.jsp?R=19890032254>.
- [23] Y. Leng, H. Yoo, T. Jardin, M. Bronz, J.-M. Moschetta, Aerodynamic modeling of propeller forces and moments at high angle of incidence, in: *AIAA Scitech 2019 Forum*, 2019.
- [24] F. Dehaeze, G. Barakos, Mesh deformation method for rotor flows, *J. Aircr.* 49 (1) (2012) 82–92, <https://doi.org/10.2514/1.C031251>.
- [25] C. Crozon, R. Steijl, G. Barakos, Coupled flight dynamics and cfd - demonstration for helicopters in shipborne environment, *Aeronaut. J.* 122 (1247) (2018) 42–82, <https://doi.org/10.1017/aer.2017.112>.
- [26] S. Babu, G. Loupy, F. Dehaeze, G. Barakos, N. Taylor, Aeroelastic simulations of stores in weapon bays using detached-eddy simulation, *J. Fluids Struct.* 66 (2016) 207–228, <https://doi.org/10.1016/j.jfluidstructs.2016.07.014>.
- [27] N. Scrase, M. Maina, The evaluation of propeller aero-acoustic design methods by means of scaled-model testing employing pressure tapped blades and spinner, in: *19th ICAS Congress, International Council of the Aeronautical Sciences, Anaheim, California, USA, ISBN 1563470845*, 1994.
- [28] A. Gomariz-Sancha, M. Maina, A. Peace, Analysis of propeller-airframe interaction effects through a combined numerical simulation and wind-tunnel testing approach, in: *53rd AIAA Aerospace Sciences Meeting, AIAA, Kissimmee, Florida*, 2015.
- [29] A. Knepper, N. Bown, *IMPACTA Wind-Tunnel Instrumentation Specification, Tech. Rep. ITS 01777, Issue 3, Dowty Propellers, GE Aviation Systems Ltd*, 2014.
- [30] G. Barakos, C. Johnson, Acoustic comparison of propellers, *Int. J. Aeroacoust.* 15 (6–7) (2016) 575–594, <https://doi.org/10.1177/1475472X16659214>.
- [31] M. Jarkowski, M. Woodgate, G. Barakos, J. Rokicki, Towards consistent hybrid overset mesh methods for rotorcraft CFD, *Int. J. Numer. Methods Fluids* 74 (8) (2014) 543–576, <https://doi.org/10.1002/flid.3861>.
- [32] D. Wilcox, *Multiscale model for turbulent flows*, *AIAA J.* 26 (11) (1988).
- [33] F. Menter, Y. Egorov, The scale-adaptive simulation method for unsteady turbulent flow predictions. Part 1: theory and model description, *Flow Turbul. Combust.* 85 (1) (2010), <https://doi.org/10.1007/s10494-010-9264-5>.
- [34] F. Menter, Two-equation eddy-viscosity turbulence models for engineering applications, *AIAA J.* 32 (8) (1994) 1598–1605, <https://doi.org/10.2514/3.12149>.
- [35] S. Babu, G. Zografakis, G. Barakos, A. Kusyumov, Evaluation of scale-adaptive simulation for transonic cavity flows, *Int. J. Eng. Syst. Model. Simul.* 8 (2) (2016), <https://doi.org/10.1504/IJESMS.2016.075510>.
- [36] G. Loupy, G. Barakos, N. Taylor, Multi-disciplinary simulations of stores in weapon bays using scale adaptive simulation, *J. Fluids Struct.* 81 (2018), <https://doi.org/10.1016/j.jfluidstructs.2018.05.012>.
- [37] R. Higgins, A. Jimenez-Garcia, G. Barakos, N. Bown, High-fidelity computational fluid dynamics methods for the simulation of propeller stall flutter, *AIAA J.* 57 (12) (2019) 5281–5292, <https://doi.org/10.2514/1.J058463>.
- [38] R. Higgins, G. Barakos, E. Jinks, Estimation of three-dimensional aerodynamic damping using cfd, *Aeronaut. J.* 124 (1271) (2019) 24–43, <https://doi.org/10.1017/aer.2019.135>.
- [39] J. Crigler, Comparison of calculated and experimental propeller characteristics for four-, six-, and eight-blade single-rotating propellers, *Wartime Report L-362, National Advisory Committee for Aeronautics*, 1944.
- [40] C. Lock, D. Yeatman, Tables for use in an improved method of airscrew strip theory calculation, *Reports and Memoranda 1674, Aeronautical Research Committee*, 1935.
- [41] S. Goldstein, On the vortex theory of screw propellers, *Proc. R. Soc. Lond. Ser. A, Contain. Pap. Math. Phys. Character* 123 (792) (1929), <https://doi.org/10.1098/rspa.1929.0078>.
- [42] J. Anderson, *Fundamentals of Aerodynamics*, 6th edition, McGraw-Hill Education, 2017.
- [43] S. Friedlander, A. Lipton-Lifschitz, Localized instabilities in fluids, in: *Handbook of Mathematical Fluid Dynamics*, North-Holland, 2003, Ch. 8.
- [44] G.J. Leishman, *Principles of Helicopter Aerodynamics*, Cambridge University Press, 2006.